

HST/NICMOS Observations of the Embedded Cluster in NGC 2024: Constraints on the IMF and Binary Fraction

Wilson M. Liu, Michael R. Meyer, Angela S. Cotera, and Erick T. Young

Steward Observatory, University of Arizona

933 N. Cherry Ave., Tucson, AZ, USA 85721

wliu@as.arizona.edu, mmeyer@as.arizona.edu, acotera@as.arizona.edu,
eyoung@as.arizona.edu

ABSTRACT

We present an analysis of NICMOS observations of the embedded cluster associated with NGC 2024. An analysis of the cluster color-magnitude diagram (CMD) using the models of D’Antona & Mazzitelli (1997) and Baraffe et al. (1998) indicates that the ratio of intermediate mass (1.0 to 10.0 M_{\odot}) to low mass (0.1 to 1.0 M_{\odot}) stars is consistent with the stellar initial mass function (IMF) for the field. In addition to the CMD analysis, we present results on the multiplicity of stars in the region. Three companions (in a sample of 95 potential primaries) were found, with angular separations between 0".4 and 1".0, translating to a projected linear separation of 184 AU to 460 AU for an estimated distance of 460 pc. The completeness of binary detections is assessed using recovery fractions calculated by a series of tests using artificially generated companions to potential primaries in the data frames. We find that the binary fraction in NGC 2024 is consistent with that of Duquennoy & Mayor (1991) for solar neighborhood stars over the range of separations and companion masses appropriate for our survey.

Subject headings: binaries: visual, open clusters and associations: individual (NGC 2024), stars: formation, stars: mass function, stars: pre-main sequence

1. Introduction

Two fundamental questions regarding star formation concern the universality of the stellar initial mass function (IMF) and the fraction of stars which exist in multiple systems at birth. More specifically, it is not known whether the functional form of the IMF is dependent on the local characteristics of a star-forming environment, or if it is universal, unchanging between different regions. A similar question exists regarding the fraction of stars observed to be in multiple systems in a star-forming region: is there a correlation between this binary fraction and the characteristics of star-forming regions, such as cluster age and central stellar density? If so, what is this correlation? NGC 2024, a young embedded cluster associated with an H II region in the Orion B giant molecular

cloud provides a good opportunity to investigate both of these aspects of star formation. The relatively high density of the cluster compared to other star-forming regions allows us to study a statistically significant sample in a small field-of-view, while the extinction through the associated cloud core is high enough to eliminate contamination from background sources. Additionally, the high resolution of the data taken with the Near-Infrared Camera and Multi-Object Spectrometer (NICMOS) onboard the *Hubble Space Telescope (HST)* presented in this study allows us to study the cluster at higher spatial resolution in the J and H-bands than previously done. These data are also complimentary to previous observations of the embedded cluster in NGC 2024 done in the I-band with the Wide Field Planetary Camera 2 onboard HST (Padgett, Strom, & Ghez 1997) and in the K-band with adaptive optics (Beck, Simon, & Close 2003, hereafter BSC03).

The IMF of several nearby star-forming regions has been well studied in recent years. The first study which investigated the field star IMF over a large range of masses ($0.1M_{\odot}$ to $10M_{\odot}$) was Miller & Scalo (1979) and has been subsequently updated by Scalo (1986) and Kroupa (2001), among others. Previous investigation into the IMF in young clusters in Orion include the near-IR study of the Trapezium by Luhman et al. (2000) as well as studies of NGC 2024 including those by Comerón, Rieke, & Rieke (1996) and Meyer (1996). These studies, along with studies of other star-forming regions, have shown evidence that the IMF is universal, unchanging regardless of local environmental conditions (Meyer et al. 2000). Our study of NGC 2024 will assess the similarity of the cluster IMF to those derived in previous studies by comparing the ratio of intermediate ($1.0-10M_{\odot}$) to low ($0.1-1.0M_{\odot}$) mass objects in NGC 2024 to the ratio expected from IMFs derived in Kroupa (2001) for the field. This ratio can be determined by using near-infrared photometry of the cluster which is then compared to theoretical models of pre-main sequence (PMS) objects, provided an estimate for the cluster age is available. As a diagnostic for the IMF, the primary advantages of using this ratio lies with the fact that the mass bins are wider than the errors in stellar mass determination from PMS models, hence the value of the ratio should be robust even with these uncertainties. However, the use of wide mass bins also makes this diagnostic insensitive to small variations in the IMF, allowing one to probe only dramatic differences between mass distributions. Nonetheless, by comparing this ratio determined for NGC 2024 to that of the Galactic field, we can probe the possibility of gross differences in the mass distribution.

The binary frequency of stellar populations has also been the focus of many recent studies, and an area of particular interest lies in determining how the binary fraction of a particular region is affected by the local environment. A study by Duquennoy & Mayor (1991) investigated solar neighborhood stars over a large mass range ($q = M_{comp}/M_{pri} = 0.1$ to 1.0) and period distribution (1 to 10^{10} days). Other studies have investigated the binary fraction in star-forming regions. Ghez, Neugebauer, & Matthews (1993) found the binary frequency in T Tauri stars in Taurus-Auriga and Ophiuchus-Scorpius to be 60 ± 17 %, about four times greater than the binary frequency derived by Duquennoy & Mayor (1991) for field stars. Padgett, Strom, & Ghez (1997) presented the binary fraction for optical sources in three clusters in Orion: NGC 2024, NGC 2068 and NGC 2071. Using WFPC2 HST observations, they found the binary fraction to be roughly equal to that of the field

over the separation range studied (138 to 1050 AU). Although it is not known exactly how the local environment affects the detected binary fraction in these clusters, there is evidence that it varies between clusters with different central stellar densities and ages (Köhler & Brandner 2001). By measuring the binary frequency in NGC 2024, we can gain further insight into the binary frequency of a region which is intermediate in central stellar density to the sparse T association of Taurus-Auriga and the rich environment of Trapezium. It also provides an independent check of the binary fraction derived for NGC 2024 by other studies, including Padgett, Strom, & Ghez (1997) and BSC03.

In this study, we present high resolution imaging of NGC 2024 obtained using NICMOS on-board *HST*. The high resolution of the dataset allows us to obtain more accurate photometry of crowded objects and those embedded in nebulosity. It also allows better sensitivity to companions at close separations. Section 2 describes the observations and data reduction procedure and presents some noteworthy features in the image. An analysis and discussion of the color-magnitude diagram (CMD) of the cluster is presented in §3, followed by the results for our binary fraction study in §4. We summarize and conclude in §5.

2. Observations and Data Reduction

Images of the young embedded cluster associated with NGC 2024 were obtained on 1998 January 17 using Camera 3 of the NICMOS (NIC3) on *HST*. Nine images, each $52''$ by $52''$, were taken with each filter (F110W and F160W) in a 3 by 3 mosaic pattern, resulting in a total field of view of $124''$ by $124''$ centered upon 05h 41m 42.4s, $-1^\circ 55' 15'' .9$. Adjacent frames overlapped by approximately $8''$ (15%). Integration times were 96 s for F110W and 80 s for F160W. These observations were taken as part of GTO/NIC program 7217 to support grism observations of the same field.

Data reduction was carried out using a combination of IRAF and custom IDL programs. The images were dark subtracted using artificial dark frames created with the *nic skydark* routine in the *nicred* package for IRAF (McLeod 1997). Each frame suffered from an offset in background level between the quadrants of the array. The offsets were determined in a manner identical to that of Luhman et al. (2000) by minimizing the median of the differences of the pixels on the borders. Using the top right quadrant as the reference quadrant, the offsets were applied to the two adjacent quadrants. The final quadrant was offset to minimize the difference with the two adjacent frames. Flat fielding was performed after correcting the quadrant offsets with flats from the Space Telescope Science Institute (STScI), also using the *nicred* data reduction package. Bad pixels in the frames (i.e., cosmic rays and other artifacts) were located initially with STScI bad pixel masks, followed by visual inspection of each frame. Aberrant pixels were replaced using the IRAF task *fixpix*, which replaces pixels using a linear interpolation of surrounding pixels. The nine images in each band were mosaicked, adjusting the background offsets for each frame in a manner similar to the quadrant offset adjustment. Figure 1 shows the final mosaicked two-color image of the central

cluster. Some interesting features and characteristics of the image are discussed in Section 2.3.

2.1. Photometry

Ninety-five sources were detected in both the F110W and F160W filters. Photometry was obtained for 79 of these sources in both bands, the remaining sources being either too bright (i.e. saturated) or too faint for accurate photometry. These sources, as well as the photometry, are presented in Table 1, and their positions are shown in Figure 2. Initial detections were made with the IRAF task *daofind* with a 10σ detection threshold. Even with the high initial threshold, each frame produced many false detections, due to a noisy background and the presence of nebulosity in the region. These spurious detections were removed through visual inspection of each frame. All final sources were detected in both the F110W and F160W frames. Photometry was extracted for each source using the *apphot* routine in IRAF. Since NIC3 undersamples the point spread function (PSF) of the sources, aperture photometry was used for all sources. Aperture corrections were calculated using several bright, isolated stars and applied to the photometry to correct for total signal. An analysis of aperture corrections versus sky noise showed the optimal aperture to be 5 pixels for most sources, with the sky background measured in an annulus from 5-7 pixels around each source. The sky annulus was measured as close as possible to the aperture so that the effect of variability from nebulosity was minimized. Apertures and sky annuli were adjusted to obtain accurate photometry of close companions (see Section 4.1 for further details about the binary detections).

Relative astrometry for each source was determined using the World Coordinate System (WCS) information in the NIC3 header with the *xy2sky* routine in the WCSTools package (Mink 2002). The derived coordinates had a fixed offset with respect to previously determined coordinates (e.g., Meyer (1996), among others). Absolute astrometry was derived by correcting for the offset using the coordinates in Meyer (1996) for the brightest sources in the field, IRS1 and IRS2, as a reference. The coordinates are presented in Table 1 and are accurate to $\lesssim 2''$, though none of the analyses in this study are dependent upon absolute astrometry. Also listed in Table 1 are the ID numbers from BSC03, if the object was detected in both studies.

2.2. Magnitude Calibration and Color Transformations

IRAF magnitudes were calibrated to the Vega system assuming 2.873×10^{-6} and 2.776×10^{-6} Jy/ADU/s and zero magnitude fluxes of 1775 and 1083 Jy for F110W and F160W respectively. Detection limits were determined using a series of artificial star tests. Artificial stars from 17th to 22nd magnitude in steps of 0.5 mag were added to each of the data frames in both bands using a PSF derived from several uncrowded sources in areas relatively free of nebulosity. The recovery fraction of our detection technique was then assessed. The 90 % completeness limits were found to

be $m_{110} \approx 19.5$ mag and $m_{160} \approx 18.0$ mag.

The NICMOS Vega magnitudes, m_{110} and m_{160} , were transformed to the ground-based CIT system, J and H. Comparisons of m_{110} vs. J, m_{160} vs. H, and $(m_{110} - m_{160})$ vs. (J - H) were made for 21 objects common to this study and a ground-based study of NGC 2024 by Meyer (1996). A linear regression was performed on these relations to obtain the following color transformations:

$$H = (0.358 \pm 0.080) + (0.935 \pm 0.006)m_{160}$$

$$(J - H) = (-0.734 \pm 0.060) + (1.05 \pm 0.02)(m_{110} - m_{160})$$

The m_{160} vs. H, and $(m_{110} - m_{160})$ vs. (J - H) relations resulted in the smallest error for the linear fit, and were therefore used to transform the NICMOS magnitudes to the ground-based CIT magnitudes, with J for each source calculated by using the transformed H-band magnitude and the (J - H) color: $J = H + (J - H)$. A J vs. (J - H) CMD of the cluster is presented in Figure 3. An analysis and discussion of the CMD will follow in the next section.

2.3. Prominent Features in the Image

Given the high resolution of the data, our images show in great detail the nebulosity and stellar distribution at the center of the cluster. There are several features worth noting. The brightest source on the west is IRS1, while IRS2 is the bright source on the east. Overall, the image shows a color gradient from east to west in both the nebulosity and stars, indicating that the east side is more deeply embedded than the west side.

The nebulosity in the region also shows interesting structure in places. The bright knot of nebulosity located about 40" southeast of the center of the field-of-view (just SE of source 1-21) has several interesting characteristics. First, the center of the knot seems to contain an extended source, possibly a deeply embedded protostellar object. It is also interesting to note that the location of the knot corresponds roughly to a compact dust condensation (FIR4) identified by Mezger et al. (1988, 1992) at 350 and 1300 μm . Previous detection of this emission have also been made at longer near-IR wavelengths (1.6 to 3.6 μm) by Moore & Chandler (1989) and Moore & Yamashita (1995) and at 450 and 800 μm by Visser et al. (1998). Two other FIR objects (FIR2 & 3) identified in the Mezger et al. (1988, 1992) are also within the field-of-view of this study; the nearby sources detected in this study are noted in Table 1. Chandler & Carlstrom (1996) performed observations of these same FIR sources at 98 and 112 GHz and found them to be consistent with extended dust emission surrounding embedded protostars as well as an outflow for FIR4.

3. The Color-Magnitude Diagram and Cluster IMF

3.1. Analysis of the CMD

Analyses of the CMD were performed in the natural NICMOS system as well as the transformed CIT magnitudes. We sought to derive a ratio of intermediate (1.0 to $10M_{\odot}$) to low (0.1 to $1.0M_{\odot}$) mass stars in order to compare it to the expected ratio for the field star IMF of Miller & Scalo (1979) and Kroupa (2001). Two sets of models were used for comparison to the cluster CMD, including the models of Baraffe et al. (1998) in both NICMOS and CIT systems, and D’Antona & Mazzitelli (1997, updated in 1998; hereafter DM98) in the CIT system, the latter of which covers objects with masses less than $0.3M_{\odot}$. Above this mass, we adopt the models of D’Antona & Mazzitelli (1994). Figure 3 shows the cluster CMD in the CIT system along with the 3×10^5 yr isochrone of DM98. An age of 3×10^5 yr was adopted for the cluster, as this was determined to be the median age of embedded objects through an analysis of the H-R diagram by Meyer (1996) using models of D’Antona & Mazzitelli (1994). The reddening vector ($A_V = 10$ mag) is also shown, (Cohen et al. 1981) as is the 90 % completeness threshold discussed above. The subsample used to calculate the ratio is extinction limited at $A_V = 18$ mag and $A_V = 17.1$ mag for the 3×10^5 yr and 1 Myr isochrones, respectively. The samples were extinction limited to ensure that we were sensitive to all masses from 0.1 to $10.0M_{\odot}$ uniformly, and not sampling massive, more luminous objects deeper into the cloud (Meyer 1996). The number of objects used in calculating the ratio for each model set ranged from 12 to 19.

Masses of objects were determined by dereddening onto an isochrone, assuming no infrared excess in the J and H-bands. In order to evaluate the possible effect of infrared excess, a (J - H) vs. (H - K) color-color diagram was created for 67 of the sources using K-band photometry from Meyer (1996) matched to sources detected in this study (Figure 4). K-band photometry for close companions unresolved in Meyer (1996) was taken from BSC03. The JHK color-color plot shows that 46 out of 67 sources are reddened main sequence (RMS) or weak-lined T Tauri stars (WTTS). Fourteen sources are classical T Tauri stars (CTTS), and seven are objects with more extreme infrared colors. In our extinction limited sample, $6/16 = 38 \pm 15$ of the sources have IR excess, which is similar to the fraction of stars with IR excess found by Meyer (1996) and Haisch, Lada, & Lada (2000). Even with the significant fraction of IR excess objects, we do not expect them to affect our results greatly. The expected J and H-band excess for a typical CTTS would result in an effect only on the order of our photometric errors (Meyer, Calvet, & Hillenbrand 1997). If the infrared excess was greater than expected, as is possible for the 7 more extreme IR-excess sources, one would expect the excess to be greater in H-band than J-band. This would lead to an over-estimation of an object’s reddening and luminosity, and therefore mass. Hence the ratio of intermediate to low mass objects would be over-estimated as well. However, the three extreme objects in the extinction limited sample have already been classified as low mass objects, therefore we are confident that these objects have been correctly characterized as low mass objects.

The ratio of intermediate to low mass objects was determined to be 0.32 ± 0.22 , consistent

with the expected ratio using the IMF presented in Miller & Scalo (1979) and Kroupa (2001) (see Section 3.2 below for further discussion). We also determined this ratio for several different isochrones in order to ascertain the effects of 1) the uncertainty in cluster age, 2) different PMS models, and 3) our color transformations. Isochrones used in this analysis included the 3×10^5 yr and 1 Myr DM98 models in the CIT magnitude system and the 1 Myr (youngest available) Baraffe et al. (1998) isochrones in both the CIT and natural NICMOS magnitude systems. For each isochrone, the ratio of intermediate to low mass objects was determined. These results are listed in Table 2 and discussed below.

Figure 5 shows a distribution of expected ratios of intermediate (1.0 to $10M_{\odot}$) to low (0.1 to $1.0M_{\odot}$) mass objects for a Miller-Scalo IMF (Miller & Scalo 1979) along with the ratios determined from the cluster CMD using the different isochrones. Ten thousand artificial samples of 20 stars were generated assuming a Miller-Scalo IMF and the relative probabilities of obtaining different ratios of intermediate to low mass stars are indicated by the vertical bars. The data points show the derived ratios for each set of models in each magnitude system. Errors shown are \sqrt{n} errors from counting the number of intermediate and low mass objects. Using the DM98 models and assuming a cluster age of 3×10^5 yr yielded good agreement between the cluster ratio and the ratio expected in a field star IMF. Adopting an older cluster age resulted in a higher fraction of intermediate mass objects in all cases, due to the luminosity evolution as a function of time for a given mass star. The Baraffe et al. (1998) isochrones result in a higher ratio of intermediate mass objects than do the DM98 isochrones. It is, however, important to note that the transformation of the pre-main sequence tracks to the observational plane were done in a different manner for the two sets of models. Baraffe et al. (1998) derived colors and magnitudes by convolving their evolutionary models with stellar atmosphere models in the CIT and NICMOS systems. The DM98 tracks were transformed to the observational plane by adopting bolometric corrections and intrinsic colors of dwarf stars (Meyer 1996, Appendix C). This difference in transformation between theoretical and observational planes may be reflected in the difference in the ratios calculated for the two sets of models. The bottom two data points show the difference in the derived ratio of intermediate to low mass objects between the CIT and NICMOS magnitude systems. These points indicate that the untransformed magnitudes in the natural NICMOS system yield a lower ratio. Again, this difference may be a result of different methods by which the models were transformed to the observational plane, or our color transformations, or both. Our results indicate that the ratio of intermediate to low mass objects in NGC 2024 is consistent with the field star IMF in the solar neighborhood for all of the models used, as well as for the CIT and NICMOS magnitude systems.

The measured ratio of intermediate to low mass objects was also compared to a theoretical value expected from the field IMF presented by Kroupa (2001). By integrating the IMF over the two appropriate mass ranges and taking the ratio of the integrals, we find a theoretical ratio of 0.199 ± 0.103 . This 1σ error was calculated for the binomial distribution (with a sample of 15 stars and a probability of success taken as $p = 0.199$, the probability of choosing an intermediate mass star). We find that our results for NGC 2024 are consistent with the ratio expected from a Kroupa

(2001) IMF.

3.2. Discussion of the CMD and IMF

Previous studies have investigated the nature of the IMF, both in the field and in star-forming regions. Our results have found that none of the models used, or ages assumed, result in a ratio of intermediate to low mass objects that is inconsistent with the field star IMF determined by Miller & Scalo (1979) or Kroupa (2001). Comerón, Rieke, & Rieke (1996) found the power law slope of the IMF in NGC 2024 to be -1.2 in linear mass units for low mass ($0.04 \lesssim M/M_{\odot} \lesssim 0.5$) objects, similar to the form of the IMF derived in Kroupa (2001) for field stars. Our results appear to confirm the agreement between the IMF in NGC 2024 and the field for stellar objects within the mass range of $0.1M_{\odot}$ to $10.0M_{\odot}$. It should be noted, however, that because our sample includes a small number of stars in the extinction limited sample, that the IMF of the region would need to differ very significantly from the field star IMF for any effect to be detectable.

Our results also show that color transformations and the different models and ages used result in small differences in the ratio of intermediate to low mass objects, but that the values agree within errors. We make no conclusions regarding the relative abundance of brown dwarfs, as our study is not sensitive to a significant number of objects with masses in the brown dwarf regime. Within the A_v -limited sample, the least massive object in our study had a mass at the hydrogen burning limit. The substellar IMF for the Trapezium (Luhman et al. 2000) and IC 348 (Najita, Tiede, & Carr 2000) have been recently investigated, and if the IMF in star-forming regions is indeed very similar, as current evidence suggests, one may expect to find a significant number of substellar objects in NGC 2024 as well.

4. The Binary Fraction

4.1. Binary Fraction Results

Each of the 95 sources detected in both bands was carefully inspected for evidence of multiplicity. Three binary candidates were identified in the sample with separations between $0''.4$ and $1''.0$ and up to a difference of 4 mag between the primary and companion. All companions were verified in both the J- and H-bands. This angular separation range translates into a projected linear separation range of 184 to 460 AU assuming a cluster distance of 460 pc. We assume that the statistical distribution of true semi-major axes is the same as the distribution of observed separations (Reipurth & Zinnecker 1993, and references therein). The outer limit of $1''.0$ was set to ensure that the probability of a coincidental superposition of stars, given the surface density of sources in the

cluster, did not exceed 1 %¹. Given the average surface density of the cluster and the 95 detected sources, it is possible that one of these candidates is a coincidental association. A difference of 4 mag between the primary and companion corresponds to a mass ratio of $q = M_{comp}/M_{pri} \approx 0.1$ at an age of 3×10^5 yr. As the 95 potential primaries ranged in mass from $\sim 0.1M_{\odot}$ to $2.3M_{\odot}$, our characteristic primary mass was taken to be $\sim 1.0M_{\odot}$. The binary candidates, their separations from their primaries, and Δm_J are listed in Table 3.

Since these binary candidates were initially detected by *daofind* as a single source, photometry was performed separately on each of the companions by visually determining the centroid of each companion, and using a smaller aperture to perform the photometry (aperture of 2 pixels with a sky annulus of 5-7 pixels). The appropriate aperture corrections were made for the new aperture size. The mass of each object was determined by dereddening onto the 3×10^5 yr DM98 isochrone, and values of q were calculated. The q values for each binary are listed in Table 3

A series of artificial star tests were performed in order to assess the competeness of our visual detection technique in identifying companions over the separations and magnitude differences described above. Artificial stars were randomly generated with a range of separations and Δm_J and placed as companions to real sources in several of the data frames. The artificial companions were then subject to the same visual inspection used to find the binary candidates. Table 5 shows the recovery fraction of artificial companions as a function of separation and difference in magnitude between the primary and companion. The number of artificially generated companions in each separation-magnitude bin was between 10 and 20 with a median of 11. None of the artificial stars generated were below the 90 % completeness limits for the photometry described in Section 2.2.

Binary detections were 90 % complete for the following range of separations and mass ratios. At 184 AU (2 pixels) we were sensitive to equal mass companions ($q = 1$). At 276 AU, $q = 0.2$ was the detection limit, and from 325 AU to 460 AU detections were sensitive down to $q = 0.1$. Over this range of separations and mass ratios, 3 binaries out of 95 potential primaries yielded a binary fraction of $0.032^{+0.018}_{-0.025}$. This error includes \sqrt{n} counting errors and the possibility of a coincidental superposition of stars.

It is interesting to compare the sample of binaries detected in this study to that of BSC03. Out of our sample of three binaries, one of them, 4-11a & b is also detected by BSC03. The derived separations are comparable, $0''.42$ in this study and $0''.39$ in the BSC03 study. The other binaries found in this study, 1-11a & b and 3-5a & b, were not resolved by BSC03, as they were not observed with AO by their study. There were also two binaries identified BSC03 not identified in this study. The first (BSC03 ID 88 & 89) only detected as a single source (ID 2-7) by this study, with no evidence of a companion. It is possible that the companion to this star is deeply embedded, hence only detected in the K-band. The other binary (BSC03 ID 54 & 55), source 7-5

¹We examined the number of companions out to $2''$ and found the number of additional associations expected from chance projections.

in this study, appears to be marginally resolved in the J-band, with some evidence of multiplicity and a separation of $\lesssim 0''.4$ in our J-band image. However, the detection was unverified in the H-band, as the brightness of the object makes it difficult to resolve close companions. Additionally, the close separation suggests that it would have fallen out of the separation range probed by this study. Three of the pairs identified by BSC03 (ID 67 & 64; 70 & 71; 70 & 72) were detected by this study, but have separations greater than the maximum separation considered. The other binaries detected by BSC03 not mentioned above fall outside of the field-of-view of our observations.

Our desire was to compare the binary fraction of NGC 2024 to that of solar neighborhood field stars determined by Duquennoy & Mayor (1991, hereafter DM91). Thus it was necessary to be certain that we were comparing equivalent separations and mass ratios between the two studies. Our study was sensitive to companions with linear projected separations of 184 to 460 AU, corresponding to an orbital period of $\log P$ [days] ≈ 6.0 to 6.5 for a characteristic system mass of $1.0M_{\odot}$. This is approximately one-half bin in Figure 7 of DM91 which shows the companion period distribution in their study. The following calculations were made to arrive at an expected number of binaries from the companion distribution in DM91 for each of our four separation bins (centered upon 184, 276, 368, and 460 AU). In the range $\log P$ [days] = 6.0 to 7.0, DM91 found a binary fraction of 8.5 %. Our separation range covers only half the DM91 bin, so the binary fraction for 184 to 460 AU was taken to be 4.25 %. There were 95 potential primaries detected in our sample, leading to a expected number of binaries to be $95 \times 0.0425 = 4$ binaries, assumed to be evenly distributed over our separation range. However, this assumes that we were sensitive to the same range of companion masses as DM91 over the entire separation range, which was not the case. To correct for this affect, we attempted to account for differences in the range of companion masses. For the mass of a typical primary in our sample ($1.0M_{\odot}$), we performed an integral of the companion mass distribution (taking the distribution to be a single power law : $\frac{dN}{dM} \sim M^{-\alpha}$) over the mass range to which we were 90 % complete. This was compared to the number of expected companions down to $q = 0.1$. The ratio between the two integrals was used to adjust the expected number of binaries in each separation bin, to account for the fact that our mass sensitivity range was smaller than that of DM91. Correcting for this difference in sensitivity to low mass companions at close separations yielded 2.9 expected binaries over our separation range. Varying the power law index of the companion mass distribution between 1.5 and 0.5 yielded between 2.7 and 3.0 binaries over our separation range. One may note that this correction for mass sensitivity only reduced the expected number of binaries by about 1, which is within the errors for the number of detected binaries given the small number of detected binaries (i.e., the number of expected binaries both before and after the correction is consistent with the observed number). However, the correction does result in a decrease of about 25% in the expected number of binaries, hence for the most accurate possible comparison between the two studies, this step is crucial. Additionally, any application of this type of mass correction to larger samples would result in a more significant effect relative to counting errors.

Our study detected $3_{-2.5}^{+1.8}$ binaries, consistent with the expected number for the solar neighbor-

hood fraction. Table 4 summarizes the expected and detected number of binaries in each separation bins assuming different functional forms of the companion mass distribution. It is interesting to note that all of our detected binaries were at close separations, while we would expect to observe more binaries in the outer separations. This is consistent with the findings of Reipurth & Zinnecker (1993) who found the distribution of companion separations (for nearby southern dark clouds) to be a steeply rising function toward smaller separations.

The binary fraction of star-forming regions in the Orion B cloud have been the focus of previous studies, including Padgett, Strom, & Ghez (1997), which presented HST WFPC2 observations of three clusters (NGC 2024, NGC 2068, and NGC 2071). They found a binary fraction of 0.15 ± 0.04 for a separation range of 138 to 1050 AU, which was about 1.3 times greater than solar neighborhood G and K stars. This suggests a slight excess of binaries in these regions; however, the significance of the excess with respect to the field was not high (Padgett, Strom, & Ghez 1997). Our results are also in agreement with BSC03 who determined the binary fraction of NGC 2024 to be similar to that of the solar neighborhood using K-band adaptive optics observations.

4.2. Discussion of the Binary Fraction

Does the local environment of a star-forming region (characteristics such as stellar density) correlate with its binary fraction? We might expect that regions of higher stellar density are subject to more frequent interactions, which would disrupt binaries and lead to a lower binary fraction. To address this question we compared our results for the binary fraction of NGC 2024 to those of other star-forming regions in order to determine how NGC 2024 fits into the context of galactic star formation. Specifically, we evaluate whether a correlation can be found between the binary fraction of a young cluster and its central stellar density.

We begin by considering the binary fraction of NGC 2024 compared to star-forming regions of lower density. Two well-studied regions which fall into this category are the Taurus star-forming region and the Rho Ophiuchus dark cloud. The stellar density of ρ Ophiuchus was determined to be more than a factor of two smaller than that of NGC 2024 (4000 pc^{-3}). The density of Taurus is smaller still (Lada et al. 1991; Lada, Strom, & Myers 1993). Ghez, Neugebauer, & Matthews (1993, hereafter GNM) performed K-band speckle imaging of the Taurus-Auriga and Ophiuchus-Scorpius star-forming regions and found a binary fraction of $60 \pm 17 \%$, about 4 times greater than DM91 for the same separation range. It is difficult to compare the binary fraction in the same *physical separation range* between these studies and ours, as the outermost separation probed by GNM is 252 AU, only 68 AU greater than the innermost separation for this study. However, in the overlap region of 184 to 252 AU, the binary fractions are $2/24 = 8.3 \pm 5.9\%$ and $1/45 = 2.2 \pm 2.2\%$ for Tau-Aur and Oph-Sco, respectively. In the overlap region, NGC 2024 has two binaries, and a binary fraction of $2/95 = 2.1 \pm 1.5\%$. While it is impossible to make a conclusive comparison due to the small sample size, the results do seem to suggest that the binary fraction of NGC 2024 is lower than that of Taurus-Auriga. Leinert et al. (1993) observed the Taurus-Auriga region with

K-band speckle imaging and found a binary fraction of 42 ± 6 %, again enhanced relative to the field star fraction of DM91. Their angular separation range of $0''.13$ to $13''$ translates to a linear projected distance of 18 to 349 AU assuming a distance of 140 pc. For the same linear separation range, DM91 found a binary fraction of about 20 %. Three low density star-forming regions in the southern sky are found in the dark clouds Chameleon, Lupus, and Corona Australis. Ghez et al. (1997) conducted a survey of these regions and found the binary fraction to be similar to Taurus and Ophiuchus, enhanced relative to the solar neighborhood (However, see Köhler (2001)). These results demonstrate that low density star-forming environments like those in Taurus seem to have significantly larger binary fractions than the environments in Orion and the field. This may indicate that the primary mode of star formation in the galaxy is not through T associations like Taurus.

The Trapezium cluster in Orion is a region of very high stellar density, about 3.5 times greater than that of NGC 2024 (Lada et al. 1991). The adaptive optics study of the Trapezium by Simon, Close, & Beck (1999) determined the binary fraction to be the same as DM91 for a separation range of 132 to 264 AU. These results were also similar to a study by Petr et al. (1998), who determined the binary fraction in the central $40'' \times 40''$ of the cluster using speckle observations in the K_s and H bands. They found that the binary fraction agreed with that of main-sequence field stars, and a factor of 3 times lower than the Taurus-Auriga star-forming region. We found that our binary fraction for NGC 2024 was roughly equivalent to that of solar neighborhood field stars over the same separation range, after being corrected for differences in mass sensitivity. Thus, with regard to the binary fraction, it appears that the intermediate density young cluster in NGC 2024 is more similar to very dense clusters like Trapezium than low density star-forming regions such as Taurus. The similarity of the binary fraction in these dense regions compared to the field suggests the possibility that most galactic field stars tend to form in denser, richer environments. However, there is some evidence to suggest that Trapezium will form a bound cluster (Kroupa, Aarseth, & Hurley 2001; Hillenbrand & Hartmann 1998) and Adams & Myers (2001) estimates only a relatively small percentage of stars ($\sim 10\%$) in the galaxy form in regions which evolve into bound clusters. This may indicate that galactic field stars form in regions of relatively high stellar density, like NGC 2024, but not so high as to form bound clusters.

Figure 6 shows the binary fraction relative to the field versus the stellar density for five different star-forming regions with ages estimated to be 2 Myr or less. It shows that young clusters of high or intermediate densities have binary fractions similar to the field while Taurus, significantly less dense than the other regions, has a binary fraction enhanced relative to the field. A linear regression to the data points yields a fit with a decreasing binary fraction with increasing density. The correlation coefficient for the fit implies a $\sim 80\%$ probability that the fitted trend is not the result of a random distribution of points, which suggests that the trend is real. While the cause of the low binary fraction in regions of higher stellar density is not known, one possibility is that binaries are disrupted by dynamical interactions. Following the argument in Binney & Tremaine (1987), the lifetime of a soft binary ($|E| < m\sigma^2$), the category in which all of the binaries in this

study fall, is on the order of several Myr. As this relation varies inversely with the density of a given star forming region, one would expect to see a decrease in binary fraction with increasing stellar density in the regime where disruptions of binaries is ongoing, that is the age of the cluster is less than the lifetime of a typical soft binary. Although the number of clusters plotted is small, and the errors fairly large, there does seem to be a trend consistent with this line of reasoning.

5. Summary and Conclusions

We have presented high resolution images of the embedded cluster in NGC 2024 taken with NICMOS onboard *HST*. Ninety-five sources were detected in the F110W and F160W bands, and photometry was extracted for 79 of these sources and transformed into m_J and m_H magnitudes in the CIT system. A color-magnitude diagram was plotted, and the masses for the sources were determined using the pre-main sequence stellar models of D’Antona & Mazzitelli (1997) and Baraffe et al. (1998). The ratio of intermediate ($1.0 - 10.0M_\odot$) to low ($0.1 - 1.0M_\odot$) mass objects was found to be consistent with a field star IMF for isochrones of 3×10^5 yr and 1 Myr.

A study of the binary fraction of the cluster was also completed. Three binary candidates were detected out of 95 potential primaries, resulting in a binary fraction of $3.2_{-2.5}^{+1.8}$ % for a linear projected separation range of 184 to 460 AU. The completeness region in separation - companion mass space was determined using a series of artificial star tests and showed the study to be complete down to $q = 0.1$ outside of 368 AU, assuming a typical primary mass of $1.0 M_\odot$. The companion mass sensitivity was reduced for closer separations. At the innermost separation of 184 AU, we were sensitive to equal mass companions. When our binary sample was corrected for differences in companion mass sensitivity, we found the binary fraction of NGC 2024 to be consistent with the solar neighborhood binary fraction determined by Duquennoy & Mayor (1991) and Kroupa (2001). A comparison to Ghez, Neugebauer, & Matthews (1993) suggests that the binary fraction of NGC 2024 is lower than that of the low density star-forming regions in Taurus-Auriga. This result supports the notion that the much of the star formation in the galaxy occurs in intermediate density clusters such as NGC 2024 and not within loose T associations like those found in Taurus.

6. Acknowledgments

WL was supported by NASA under the NICMOS grant to the University of Arizona. MRM is very grateful for support from the Lucas Foundation, and NASA grants HF-01098.01-97A and GF-7417 awarded by the Space Telescope Science Institute which is operated by the Association of Universities for Research in Astronomy, Inc. for NASA under contract NAS 5-26555. The authors also thank the referee for helpful comments.

REFERENCES

- Adams, F. C. & Myers, P. C. 2001, *ApJ*, 553, 744
- Baraffe, I., Chabrier, G., Allard, F., & Hauschildt, P. H. 1998, *A&A*, 337, 403
- Beck, T. L., Simon, M., & Close, L. M. 2003, *ApJ*, 583, 358
- Binney, J. & Tremaine, S. 1987, Princeton, NJ, Princeton University Press, 1987, 747 p.
- Brandner, W., Alcalá, J. M., Kunkel, M., Moneti, A., & Zinnecker, H. 1996, *A&A*, 307, 121
- Chandler, C. J. & Carlstrom, J. E. 1996, *ApJ*, 466, 338
- Cohen, J. G., Persson, S. E., Elias, J. H., & Frogel, J. A. 1981, *ApJ*, 249, 481
- Comeron, F., Rieke, G. H., & Rieke, M. J. 1996, *ApJ*, 473, 294
- D'Antona, F. & Mazzitelli, I. 1994, *ApJS*, 90, 467
- D'Antona, F. & Mazzitelli, I. 1997, *Memorie della Societa Astronomica Italiana*, 68, 807
- Duquennoy, A. & Mayor, M. 1991, *A&A*, 248, 485
- Ghez, A. M., Neugebauer, G., & Matthews, K. 1993, *AJ*, 106, 2005
- Ghez, A. M., McCarthy, D. W., Patience, J. L., & Beck, T. L. 1997, *ApJ*, 481, 378
- Haisch, K. E., Lada, E. A., Piña, R. K., Telesco, C. M., & Lada, C. J. 2001, *AJ*, 121, 1512
- Haisch, K. E., Lada, E. A., & Lada, C. J. 2000, *AJ*, 120, 1396
- Hester, J. J. et al. 1996, *AJ*, 111, 2349
- Hillenbrand, L. A. & Hartmann, L. W. 1998, *ApJ*, 492, 540
- Köhler, R. 2001, *AJ*, 122, 3325
- Köhler, R. & Brandner, W. 2001, *IAU Symposium*, 200, 147
- Kroupa, P. 2001, *MNRAS*, 322, 231
- Kroupa, P., Aarseth, S., & Hurley, J. 2001, *MNRAS*, 321, 699
- Kroupa, P., Petr, M. G., & McCaughrean, M. J. 1999, *New Astronomy*, 4, 495
- Kroupa, P., Tout, C. A., & Gilmore, G. 1993, *MNRAS*, 262, 545
- Lada, E. A., Evans, N. J., Depoy, D. L., & Gatley, I. 1991, *ApJ*, 371, 171
- Lada, E. A., Strom, K. M., & Myers, P. C. 1993, *Protostars and Planets III*, 245

- Leinert, C., Zinnecker, H., Weitzel, N., Christou, J., Ridgway, S. T., Jameson, R., Haas, M., & Lenzen, R. 1993, *A&A*, 278, 129
- Luhman, K. L., Rieke, G. H., Young, E. T., Cotera, A. S., Chen, H., Rieke, M. J., Schneider, G., & Thompson, R. I. 2000, *ApJ*, 540, 1016
- Mathieu, R. D., Ghez, A. M., Jensen, E. L. N., & Simon, M. 2000, *Protostars and Planets IV*, 703
- McLeod, B. A. 1997, *The 1997 HST Calibration Workshop with a new generation of instruments* /edited by Stefano Casertano, Robert Jedrzejewski, Charles D. Keyes, and Mark Stevens. Baltimore, MD : Space Telescope Science Institute (1997) QB 500.268 C35 1997, p. 281., 281
- Mezger, P. G., Chini, R., Kreysa, E., Wink, J. E., & Salter, C. J. 1988, *A&A*, 191, 44
- Mezger, P. G., Sievers, A. W., Haslam, C. G. T., Kreysa, E., Lemke, R., Mauersberger, R., & Wilson, T. L. 1992, *A&A*, 256, 631
- Meyer, M. R. 1996, Ph.D. Thesis, University of Massachusetts
- Meyer, M. R., Calvet, N., & Hillenbrand, L. A. 1997, *AJ*, 114, 288
- Meyer, M. R., Adams, F. C., Hillenbrand, L. A., Carpenter, J. M., & Larson, R. B. 2000, *Protostars and Planets IV*, 121
- Miller, G. E. & Scalo, J. M. 1979, *ApJS*, 41, 513
- Mink, D. J. 2002, *ASP Conf. Ser. 281: Astronomical Data Analysis Software and Systems XI*, 11, 169
- Moore, T. J. T. & Yamashita, T. 1995, *ApJ*, 440, 722
- Moore, T. J. T. & Chandler, C. J. 1989, *MNRAS*, 241, 19P
- Najita, J. R., Tiede, G. P., & Carr, J. S. 2000, *ApJ*, 541, 977
- Padgett, D. L., Strom, S. E., & Ghez, A. 1997, *ApJ*, 477, 705
- Petr, M. G., Coude Du Foresto, V., Beckwith, S. V. W., Richichi, A., & McCaughrean, M. J. 1998, *ApJ*, 500, 825
- Reipurth, B. & Zinnecker, H. 1993, *A&A*, 278, 81
- Scalo, J. M. 1986, *Fundamentals of Cosmic Physics*, 11, 1
- Simon, M., Close, L. M., & Beck, T. L. 1999, *AJ*, 117, 1375
- Visser, A. E., Richer, J. S., Chandler, C. J., & Padman, R. 1998, *MNRAS*, 301, 585

Fig. 1.— Two-color (F110W and F160W) image of the young embedded cluster in NGC 2024. The field-of-view is just over $2' \times 2'$. North is up and east is to the left.

Fig. 2.— Distribution of sources detected in the J and H bands. Frame numbers are shown in the upper-right corner of each frame. Plate scale is ≈ 0.2 arcsec per pixel and each frame overlaps adjacent frames by ≈ 40 pixels. The center of Frame 1 is located at 05h 41m 42.4s, $-1^\circ 55' 15''.9$

Fig. 3.— The CMD of the cluster in the CIT magnitude system. Also shown are the 300,000 yr (DM98) isochrone, $0.1 M_\odot$ extinction limit, and 90 % completeness limit.

Fig. 4.— Color-color diagram for 67 objects in the sample. Forty-six are reddened main sequence (RMS) or weak-lined T Tauri stars (WTTS), 14 are classical T Tauri stars (CTTS) and 7 are objects with more extreme colors. K-band data was taken from Meyer (1996) and Beck, Simon, & Close (2003). The CTTS locus is that of Meyer (1996) and the stellar models are those of D’Antona & Mazzitelli (1994)

Fig. 5.— The ratio of intermediate to low mass objects in the cluster as determined by this study (data points and errors), and a distribution of ratios predicted by a Miller -Scalo IMF (MS79) for 20 objects (vertical bars). The vertical spacing of the data points is arbitrary.

Fig. 6.— The binary fraction relative to the field vs. stellar density for five young star-forming regions. Density data was taken from Table 1 of Meyer et al. (2000) and binary fractions are those compiled in Table 1 of Mathieu et al. (2000), except for NGC 2024 which reflects the value found in this study.

Table 1. Objects Dectected in J and H bands

Frame-ID	X	Y	RA (J2000)	Dec (J2000)	J	J-error	H	H-error	BSC03 ID	Notes
1-1	71.0	21.0	05 41 41.30	-1 53 51.9	17.42	0.35	13.62	0.14	66	proximity to FIR2
1-2	233.0	29.0	5 41 43.49	-1 53 56.3	18.85	0.59	14.85	0.18	N/A	
1-3	200.8	34.6	5 41 43.04	-1 53 56.9	18.81	0.58	15.00	0.18	79	
1-4	161.0	66.0	5 41 42.47	-1 54 2.6	16.81	0.29	13.55	0.14	75	proximity to FIR3
1-5	160.1	99.9	5 41 42.42	-1 54 9.4	15.11	0.20	12.51	0.13	74	
1-6	43.1	104.4	5 41 40.82	-1 54 8.3	20.74	1.32	16.01	0.23	N/A	
1-7	98.5	117.5	5 41 41.56	-1 54 11.9	17.69	0.38	14.04	0.15	70	
1-8	107.0	118.0	5 41 41.68	-1 54 12.2	18.05	0.44	14.84	0.18	72	
1-9	214.9	120.3	5 41 43.14	-1 54 14.5	19.05	0.69	16.29	0.25	81	
1-10	102.8	124.7	5 41 41.61	-1 54 13.5	17.52	0.36	14.19	0.16	71	proximity to FIR4
1-11a	128.6	172.8	5 41 41.91	-1 54 23.7	16.77	0.22	12.98	0.13	73	
1-11b	130.0	176.0	5 41 41.92	-1 54 24.4	18.67	0.36	15.10	0.16	73	
1-12	225.6	215.2	5 41 43.17	-1 54 34.0	17.01	0.32	14.42	0.16	82	
1-13	194.3	227.4	5 41 42.74	-1 54 35.9	14.71	0.18	12.06	0.12	78	
1-14	77.6	48.0	5 41 41.36	-1 53 57.5	21.30	1.77	17.34	0.34	68	
2-1	147.0	17.0	5 41 45.33	-1 53 56.2	N/A	N/A	N/A	N/A	N/A	
2-2	65.9	68.0	5 41 44.17	-1 54 5.2	18.56	0.51	14.26	0.16	N/A	
2-3	127.7	68.7	5 41 45.01	-1 54 6.4	17.60	0.36	12.94	0.13	N/A	
2-4	191.1	86.4	5 41 45.85	-1 54 11.1	N/A	N/A	13.02	0.13	N/A	
2-5	209.0	103.9	5 41 46.07	-1 54 14.9	N/A	N/A	14.56	0.17	93	
2-6	82.6	141.4	5 41 44.32	-1 54 20.3	17.21	0.33	13.75	0.15	84	
2-7	147.6	148.9	5 41 45.19	-1 54 23.0	17.14	0.32	13.39	0.14	88,89	
2-8	168.0	175.5	5 41 45.44	-1 54 28.7	N/A	N/A	N/A	N/A	90	
2-9	123.8	214.9	5 41 44.79	-1 54 35.9	15.99	0.24	12.71	0.13	86	
2-10	83.1	26.8	5 41 44.45	-1 53 57.1	21.70	2.19	17.02	0.31	N/A	

Table 1—Continued

Frame-ID	X	Y	RA (J2000)	Dec (J2000)	J	J-error	H	H-error	BSC03 ID	Notes
2-11	118.0	162.0	5 41 44.77	-1 54 25.1	12.97	0.15	10.61	0.11	85	
2-12	192.0	179.0	5 41 45.76	-1 54 29.8	N/A	N/A	N/A	N/A	92	IRS2
3-1	151.2	47.0	5 41 45.10	-1 54 47.3	15.05	0.19	11.88	0.12	87	
3-2	148.8	85.3	5 41 45.02	-1 54 55.0	18.76	0.56	14.69	0.17	N/A	
3-3	90.6	93.0	5 41 44.23	-1 54 55.6	19.62	0.80	15.31	0.19	N/A	
3-4	200.6	96.9	5 41 45.71	-1 54 58.3	18.65	0.61	16.23	0.24	N/A	
3-5a	219.0	114.0	5 41 45.94	-1 55 2.1	16.66	0.29	13.23	0.14	N/A	
3-5b	220.0	115.0	5 41 45.96	-1 55 2.4	16.58	0.28	13.34	0.14	N/A	
3-6	172.8	122.6	5 41 45.31	-1 55 3.0	17.36	0.35	13.80	0.15	N/A	
3-7	201.0	131.0	5 41 45.68	-1 55 5.2	17.36	0.34	13.85	0.16	N/A	
3-8	79.7	154.2	5 41 44.01	-1 55 7.8	18.81	0.59	15.32	0.19	N/A	
3-9	96.3	216.6	5 41 44.16	-1 55 20.8	18.58	0.52	14.44	0.16	N/A	
3-10	113.2	228.0	5 41 44.38	-1 55 23.4	13.44	0.16	11.25	0.11	N/A	
3-11	109.0	237.1	5 41 44.31	-1 55 25.1	14.65	0.19	12.94	0.13	N/A	
4-1	198.1	24.9	5 41 42.77	-1 54 39.8	17.93	0.45	15.43	0.20	77	
4-2	104.1	32.9	5 41 41.48	-1 54 39.8	15.96	0.23	12.81	0.13	67	
4-3	117.2	37.2	5 41 41.65	-1 54 40.9	19.98	1.02	16.17	0.24	69	
4-4	99.0	59.3	5 41 41.38	-1 54 45.1	17.75	0.39	13.69	0.15	65	
4-5	135.9	132.9	5 41 41.80	-1 55 0.6	17.21	0.33	13.99	0.15	N/A	
4-6	185.0	141.2	5 41 42.45	-1 55 3.2	15.94	0.23	12.68	0.13	N/A	
4-7	169.3	179.0	5 41 42.20	-1 55 10.6	12.74	0.15	11.20	0.11	N/A	
4-8	55.6	231.9	5 41 40.59	-1 55 19.3	15.70	0.22	12.83	0.13	N/A	
4-9	38.9	251.7	5 41 40.35	-1 55 23.1	21.43	2.21	16.76	0.29	N/A	
4-10	190.0	57.1	5 41 42.62	-1 54 46.2	14.80	0.19	12.380	0.12	N/A	
4-11a	95.3	25.0	5 41 41.37	-1 54 38.1	18.30	0.51	15.11	0.19	63	

Table 1—Continued

Frame-ID	X	Y	RA (J2000)	Dec (J2000)	J	J-error	H	H-error	BSC03 ID	Notes
4-11b	93.8	26.5	5 41 41.35	-1 54 38.4	18.50	0.55	15.32	0.20	64	
5-1	187.4	57.3	5 41 39.59	-1 54 42.4	18.15	0.46	14.59	0.17	57	
5-2	91.9	131.4	5 41 38.20	-1 54 55.8	14.90	0.19	12.80	0.13	40	
5-3	158.9	155.0	5 41 39.09	-1 55 1.7	17.20	0.34	14.65	0.17	N/A	
5-4	169.6	179.3	5 41 39.20	-1 55 6.8	19.79	1.25	18.54	0.55	N/A	
5-5	65.6	207.0	5 41 37.76	-1 55 10.6	16.32	0.27	14.67	0.17	31	
5-6	53.1	66.0	5 41 37.75	-1 54 41.9	13.25	0.15	11.79	0.12	32	
5-7	58.5	42.5	5 41 37.85	-1 54 37.2	N/A	N/A	N/A	N/A	33	IRS1
6-1	32.7	45.2	5 41 37.75	-1 53 52.3	N/A	N/A	N/A	N/A	30	
6-2	60.0	71.3	5 41 38.09	-1 53 58.1	13.34	0.15	11.54	0.12	37	
6-3	135.0	70.6	5 41 39.11	-1 53 59.2	N/A	N/A	N/A	N/A	50	
6-4	148.7	88.0	5 41 39.28	-1 54 3.0	16.51	0.28	14.59	0.17	52	
6-5	220.8	108.1	5 41 40.23	-1 54 8.3	N/A	N/A	14.11	0.15	60	
6-6	149.3	147.7	5 41 39.22	-1 54 15.1	14.01	0.17	11.12	0.11	51	
6-7	79.8	170.7	5 41 38.25	-1 54 18.6	17.43	0.40	15.51	0.20	42	
6-8	101.0	207.1	5 41 38.50	-1 54 26.3	11.01	0.13	11.28	0.11	46	
6-9	121.1	224.4	5 41 38.75	-1 54 30.2	17.03	0.32	14.34	0.16	48	
6-10	39.0	209.1	5 41 37.65	-1 54 25.7	12.49	0.14	11.09	0.11	28	
7-1	123.6	44.0	5 41 39.24	-1 53 8.7	17.98	0.43	14.63	0.17	53	
7-2	135.4	70.8	5 41 39.37	-1 53 14.4	19.16	0.86	17.89	0.41	N/A	
7-3	84.0	122.7	5 41 38.62	-1 53 24.0	N/A	N/A	N/A	N/A	47	
7-4	225.0	133.0	5 41 40.52	-1 53 28.5	N/A	N/A	15.52	0.20	N/A	
7-5	152.5	136.9	5 41 39.53	-1 53 28.1	13.36	0.16	10.82	0.11	54,55	possible close binary
7-6	53.0	139.0	5 41 38.18	-1 53 26.8	16.52	0.29	14.85	0.18	39	
7-7	67.0	152.0	5 41 38.35	-1 53 29.6	15.93	0.24	14.08	0.15	44	

Table 1—Continued

Frame-ID	X	Y	RA (J2000)	Dec (J2000)	J	J-error	H	H-error	BSC03 ID	Notes
7-8	207.0	168.5	5 41 40.23	-1 53 35.4	14.87	0.19	11.97	0.12	N/A	
7-9	155.9	170.6	5 41 39.54	-1 53 34.9	15.18	0.20	12.56	0.13	56	
7-10	69.2	175.0	5 41 38.36	-1 53 34.4	12.87	0.15	12.57	0.13	45	
7-11	198.2	176.1	5 41 40.10	-1 53 36.8	15.30	0.20	12.71	0.13	58	
7-12	187.7	199.0	5 41 39.94	-1 53 41.3	18.03	0.48	15.95	0.23	N/A	
7-13	245.5	235.4	5 41 40.68	-1 53 49.6	18.17	0.46	14.60	0.17	N/A	
7-14	53.0	57.7	5 41 38.27	-1 53 10.3	11.88	0.14	10.14	0.11	43	
7-15	38.0	106.7	5 41 38.01	-1 53 20.0	15.76	0.24	14.25	0.16	36	
7-16	29.0	70.1	5 41 37.93	-1 53 12.4	11.28	0.13	10.41	0.11	35	
8-1	197.8	73.0	5 41 43.21	-1 53 19.7	N/A	N/A	N/A	N/A	N/A	
8-2	216.5	129.9	5 41 43.40	-1 53 31.6	N/A	N/A	14.89	0.18	N/A	
8-3	71.4	155.1	5 41 41.41	-1 53 34.2	19.24	0.66	14.05	0.15	N/A	
8-4	53.0	160.2	5 41 41.15	-1 53 34.9	20.52	1.26	16.58	0.27	N/A	
9-1	38.0	123.0	5 41 44.00	-1 53 30.9	N/A	N/A	13.96	0.15	N/A	
9-2	141.2	140.7	5 41 45.37	-1 53 36.3	19.28	0.74	16.26	0.24	N/A	
9-3	57.6	162.3	5 41 44.21	-1 53 39.2	N/A	N/A	15.01	0.18	N/A	
9-4	187.1	187.7	5 41 45.94	-1 53 46.6	16.72	0.29	14.03	0.15	N/A	
9-5	214.0	194.9	5 41 46.29	-1 53 48.5	13.94	0.17	11.39	0.12	N/A	
9-6	61.0	210.8	5 41 44.20	-1 53 49.1	N/A	N/A	15.28	0.19	N/A	
9-7	107.2	212.4	5 41 44.82	-1 53 50.2	N/A	N/A	15.33	0.19	N/A	
9-8	47.3	231.8	5 41 44.00	-1 53 53.1	N/A	N/A	15.02	0.18	N/A	
9-9	58.449	186.4	5 41 44.19	-1 53 44.1	N/A	N/A	17.24	0.33	N/A	
9-10	75.1	153.1	5 41 44.45	-1 53 37.6	N/A	N/A	N/A	N/A	N/A	

Table 2. Ratio of Intermediate to Low Mass Objects

Model Set	Reference	Age (Myr)	Mag. System	$\frac{N(1-10M_{\odot})}{N(0.1-1M_{\odot})}$
1	D’Antona & Mazzitelli (1997)	0.3	CIT	0.31 ± 0.22
2	D’Antona & Mazzitelli (1997)	1.0	CIT	0.67 ± 0.43
3	Baraffe et al. (1998)	1.0	CIT	1.00 ± 0.63
4	Baraffe et al. (1998)	1.0	NICMOS	0.88 ± 0.64

Table 3. Binary Candidates Identified

ID	Separation (")/AU	m_J (primary)	Δm_J	$q = \frac{M_{comp}}{M_{pri}}$
1-11(a,b)	0.70 / 321	16.77	1.91	0.14
3-5(a,b)	0.36 / 166	16.58	0.08	0.73
4-11(a,b)	0.42 / 195	18.30	0.20	0.92

Table 4. Expected and Detected Binaries

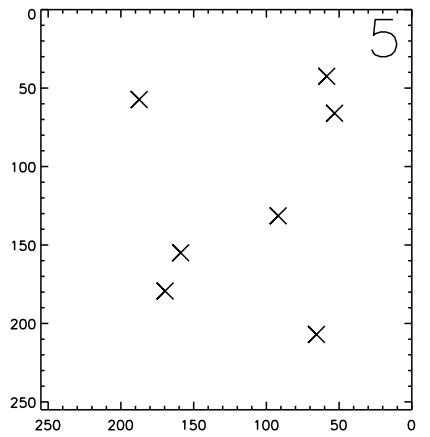
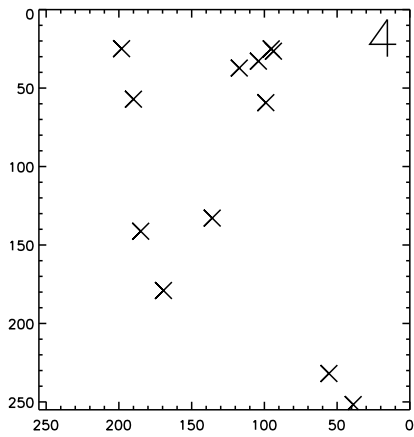
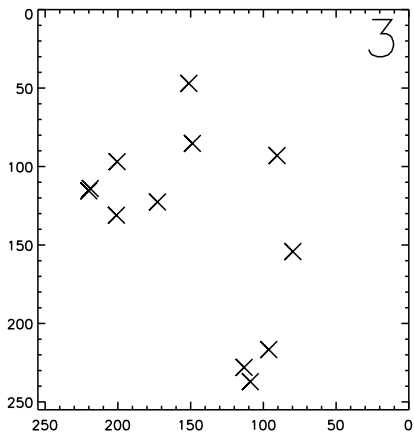
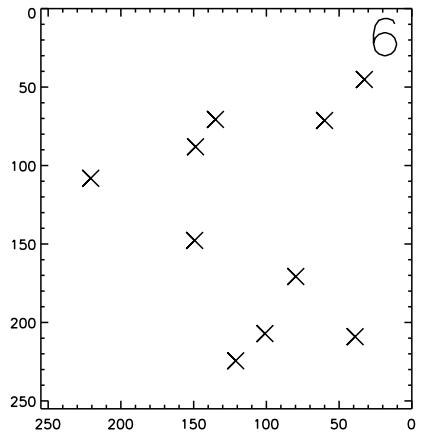
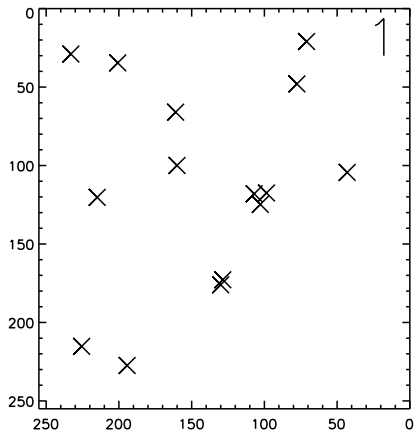
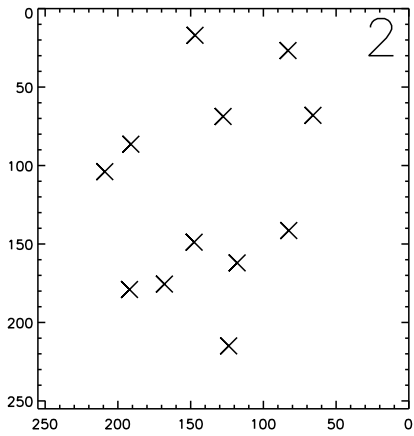
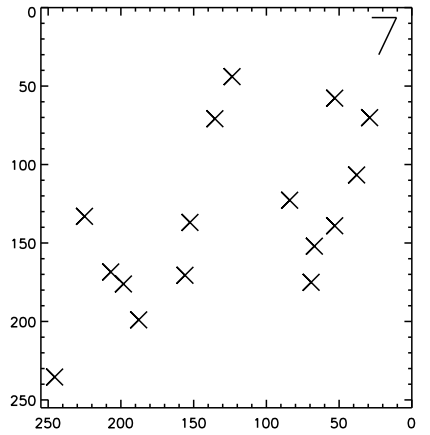
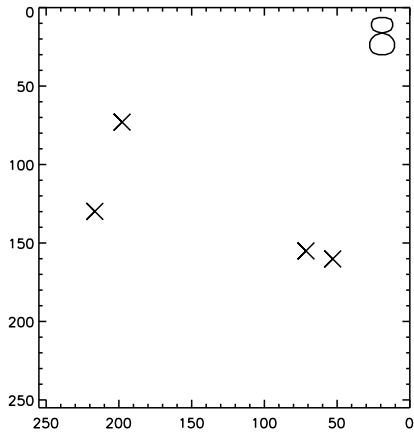
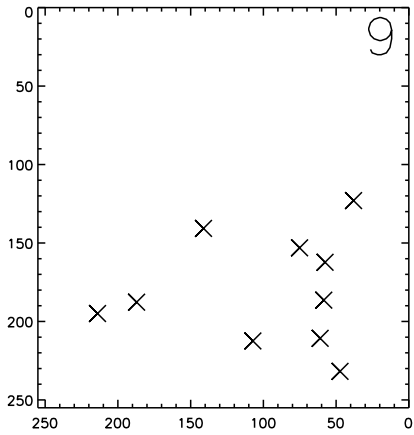
Separation (")/AU	Detected	Expected ($\alpha = 0.5$)	($\alpha = 1.0$)	($\alpha = 1.5$)
0.4 / 184	2	0.2	0.2	0.1
0.6 / 276	1	0.8	0.7	0.6
0.8 / 368	0	1.0	1.0	1.0
1.0 / 460	0	1.0	1.0	1.0
Total	3	3.0	2.9	2.7

Table 5. Binary Completeness - Recovery Fraction

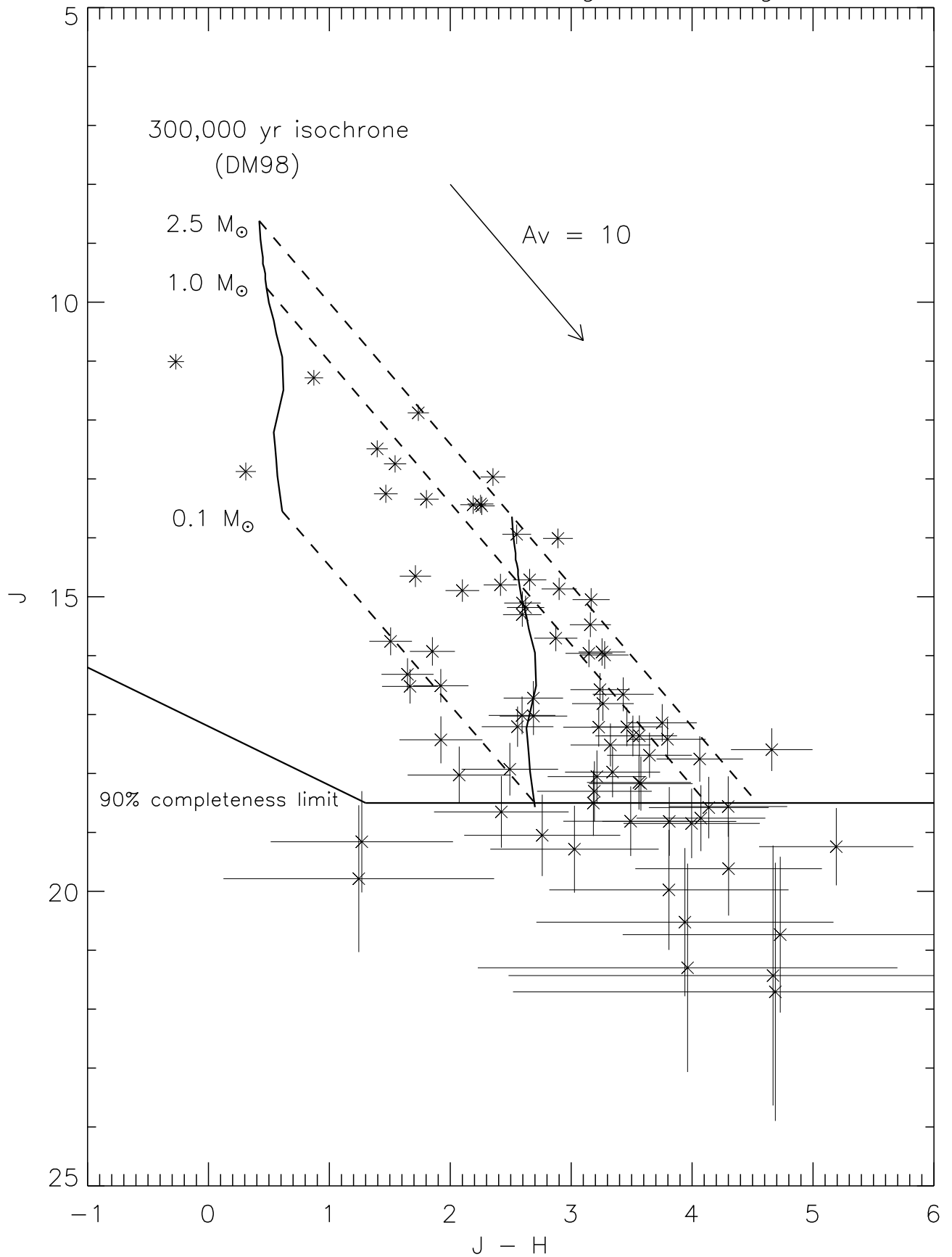
Δm_J	1 pix / 92 AU	2 / 184	3 / 276	4 / 368	5 / 460
0	0.000	0.909	1.000	1.000	1.000
1	0.000	0.727	0.950	1.000	1.000
2	0.000	0.364	0.909	1.000	1.000
3	0.000	0.000	0.500	1.000	1.000
4	0.000	0.000	0.200	0.583	0.833
5	0.000	0.000	0.000	0.091	0.250

This figure "figure1.jpg" is available in "jpg" format from:

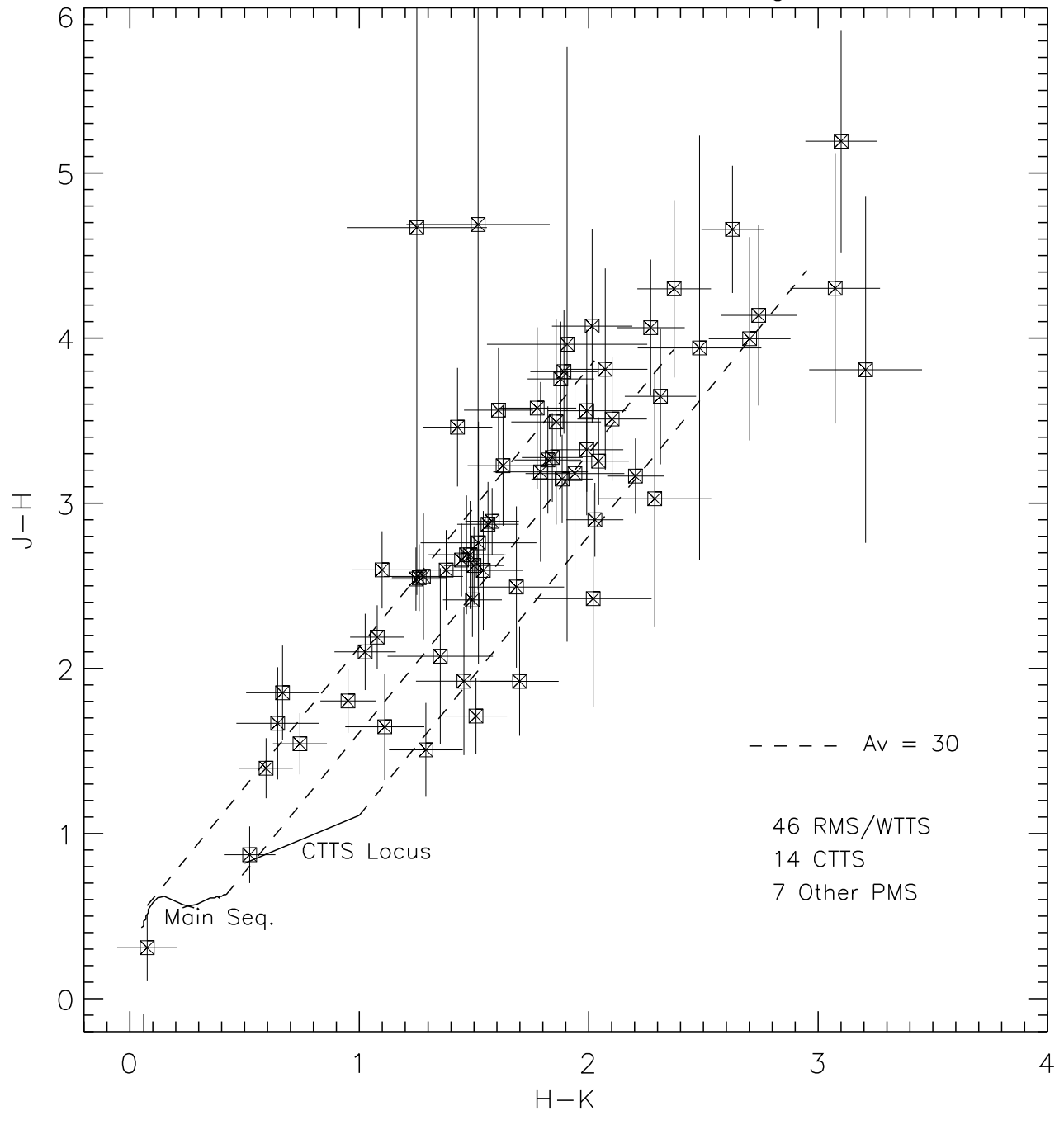
<http://arxiv.org/ps/astro-ph/0306377v1>



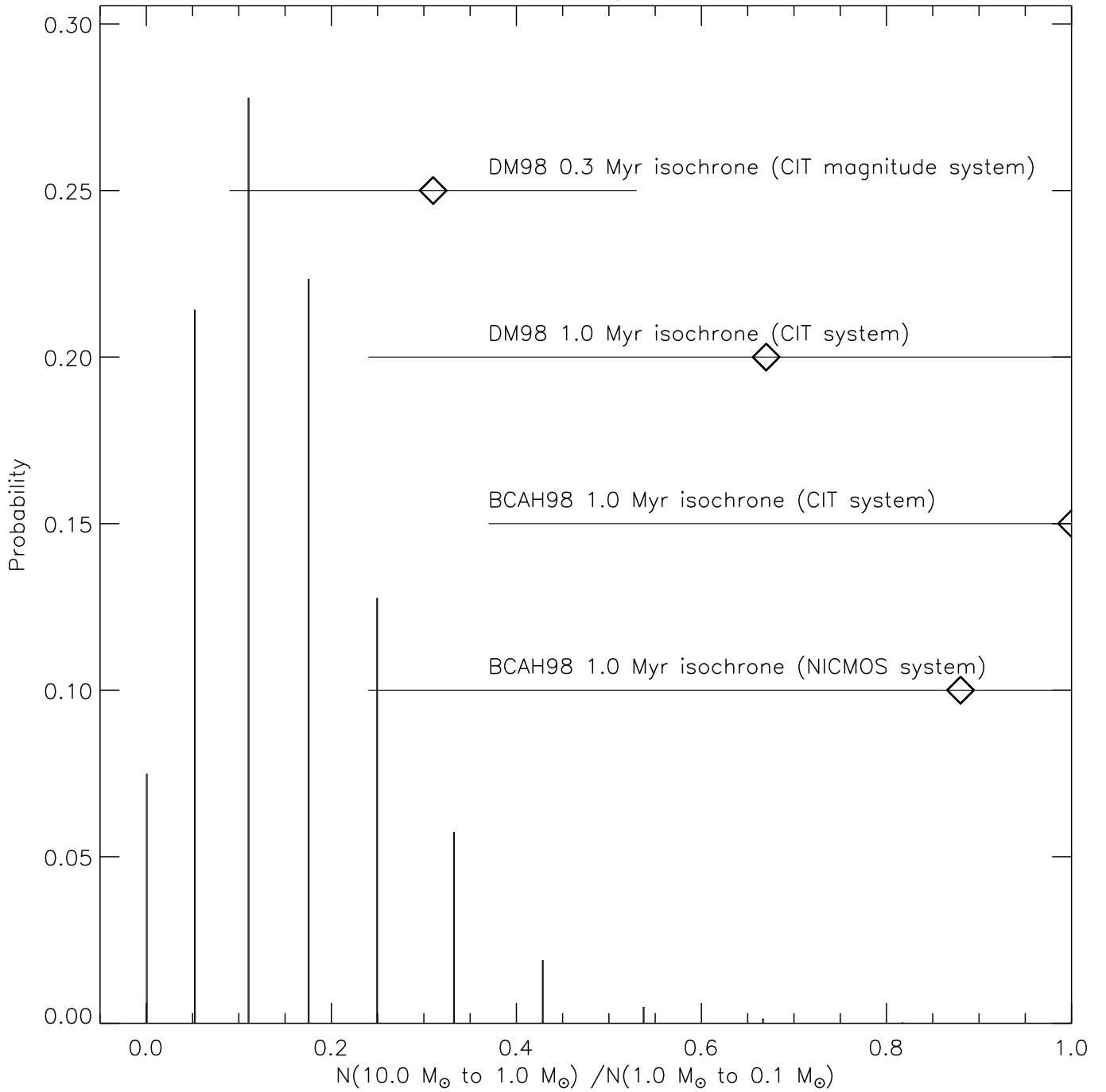
NGC 2024: CIT Color–Magnitude Diagram



NGC 2024: Color-Color Diagram



Predicted Ratio for Miller–Scalo IMF (20 stars sampled 10,000 times)



Binary Fractions of Young Clusters

